Investigation of Thermo-optical Nonlinearity in Graphene

PH5101
MS report

Submitted by
Abhijeet Kumar
13MS027

Supervisor
Dr. Bipul Pal

December 7, 2017

Contents

Abstract

Liquid suspension of graphene and graphene oxide nanoparticles provides excellent example of their strong nonlinear optical properties through Spatial Self-Phase Modulation (SSPM). However, the origin of SSPM in graphene is still not clear and demands deeper analysis. Since both electronic and thermal heat due to laser contribute to nonlinearity in graphene, it gets challenging to distinguish them. We observe SSPM in graphene and graphene oxide over large wavelength regime (ultraviolet, visible and near-infrared), and perform some control experiments to observe the dominance of one or the other. The obtained results hint at a dominating thermal convection in graphene during SSPM. The estimated value of optical properties such as nonlinear refractive index and nonlinear susceptibility in graphene and graphene oxide match quite well with those reported in literature. Further investigations are going on to reach a conclusion about the main contributor to SSPM in graphene.

Chapter 1

Introduction

Nonlinear optics deals with the study of phenomena occurring as a consequence of the modification of the optical properties of a material due to the presence of intense light. By high intensity we mean that the incident electric field is as strong as to disturb the inter-atomic electric field in material. These phenomena are nonlinear because the material responds to the applied field in a nonlinear manner. At high intensity, the interaction between light and matter is quite strong and it modifies the properties of light [1]. Intensity dependent optical properties of material fall under the category of nonlinear phenomena. Generally, lasers create high intensity electric field and therefore are used to study optical nonlinearities in a system.

Spatial Self-Phase Modulation (SSPM) is one such property of a material, where its refractive index depends on the intensity of incident light. In $Chapter2$, we study in detail, the physics of SSPM and nonlinearity arose due to SSPM.

In this work, we have studies optical nonlinearities in graphene and graphene oxide sispersion using SSPM. Graphene is a 2-D allotrope of carbon with zero band-gap [2]. This allows us to perform optical studies on graphene over a large wavelength regime. Graphene was prepared using electrochemical exfoliation of graphite sheets, while graphene oxide was prepared by modified Hummer's method. We estimate nonlinear optical properties of graphene such as nonlinear refractive index and nonlinear susceptibility of graphene and graphene oxide dispersion. These values are well within acceptance rate with those reported elsewhere ($Chapter2$).

As laser propagates through a nonlinear liquid medium, it generates significant amount of heat and causes thermal effect, which in turn modifies nonlinearity of the medium. Main aim of our work is to distinguish thermal nonlinearity in graphene from its electronic origin and to show that the thermal effect dominates over the electronic effect while causing nonlinearity in graphene dispersion. We do observe experimentally, a significant impact of thermal effect on nolinear properties of graphene. However, current results are not conclusive enough to declare SSPM in graphene as a thermal effect. Therefore we aim to investigate deep in this direction.

Chapter 2

Spatial Self-Phase Modulation

2.1 Intensity Dependent Refractive Index

The refractive index of many optical materials depend on the intensity of the incident electric field. This is known as optical Kerr effect (was first proposed for liquids where molecules undergo reorientation and alignment under applied electric field) and can be described by the relation

$$n_e = n_{0e} + n_{2e} I \tag{2.1}$$

where n_{0e} is the linear refractive index, n_{2e} is the nonlinear refractive index of material and I is the incident intensity [1].

In nonlinear optics, total polarization of a material is given by

$$P(t) = \epsilon_0[\chi^{(1)}E(t) + \chi^{(2)}E^2(t) + \chi^{(3)}E^3(t) + ...] \tag{2.2}$$

For a centrosymmetric material, such as graphene ($P(t) = P(-t)$), we write

$$P(t) = \epsilon_0\chi^{(1)}E(t) + \epsilon_0\chi^{(3)}E^3(t)$$

Using the relation $n^2 = 1 + \chi$ we can obtain the relation between nonlinear refractive index and nonlinear susceptibility as

$$n_{2e}(\frac{m^2}{W}) = \frac{3}{4n_{0e}^2\epsilon_0 c}\chi^3(\frac{m^2}{v^2}) = \frac{395}{n_{0e}^2}\chi^3(esu) \tag{2.3}$$

2.1.1 Self-Focusing and Self-Defocusing

Self focusing and self defocusing (also called self action) is a charecteristic of Gaussian beam that occur as a result of intensity dependent refractive index. A Gaussian beam has nonuniform transverse intensity distribution to its direction of propagation in a way that the intensity is maximum at the center of the laser spot and decreases radially outward. From the intensity dependence of refractive index (2.1), it is evident that the speed of Gaussian beam will vary in radial direction from its center point along the axis of propagation. If the nonlinear refractive index of medium is negative, then the speed of beam will be higher in its central region than the surrounding radial region. Hence the medium will behave as concave lens and the beam will get defocused along the axis. If n_{2e} of the medium is positive, speed of the central region will be lower than the surrounding, consequently, the medium will act as convex lens and self focusing occurs.

2.2 Spatial Self-Phase Modulation (SSPM)

As seen from (2.1), the refractive index is a function of intensity of light. Since the Gaussian beam has a nonuniform intensity profile, this creates a refractive index variation of the material inside the pulse itself. The center of the pulse sees a large refractive index and it decreases as one goes either side of the center. With the moving Gaussian beam, this refractive index profile too moves inside the sample. This leads to the change in velocity and hence a change in phase. Because this spatial phase difference inside the beam is caused due to beam itself is called spatial self-phase modulation (SSPM). The phase difference at different spatial points results in a pattern of concentric diffraction rings in far field as the beam transmits through the medium. Whether the interference between two beams propagating from two different points will be constructive or destructive is determined by whether the phase difference is even or odd multiple of π (figure 2.1).

2.3 Nonlinear Properties Using SSPM

Let us consider a Gaussian laser beam of beam waist (w_0) propagating through a nonlinear medium of thickness L along z-axis. The complex electric field

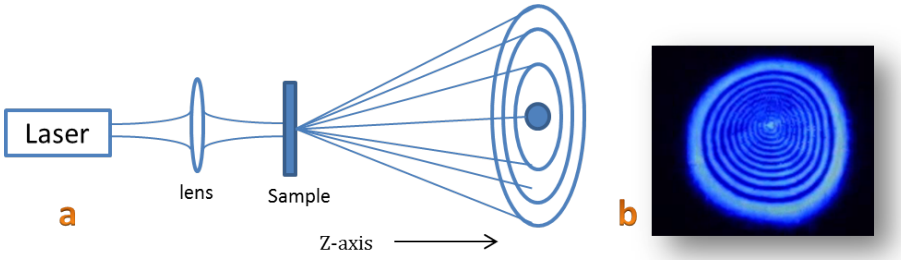

Figure 2.1: a) Schematic diagram of experimental set up for SSPM. b) Experimentally observed diffraction ring pattern.

amplitude of the Gaussian beam is given by

$$E(r,z) = E(0,z)\frac{w_0}{w(z)}\exp(-\frac{r^2}{w(z)^2})\exp(-i[kz - arctan\frac{z}{z_R} + \frac{kn_0r^2}{2R(z)}]) \quad (2.4)$$

where $E(0,z)$ is the peak electric field amplitude, w_0 is beam waist, $k = 2\pi/\lambda$ is wavenumber, z_R is Rayleigh length and $R(z)$ is the redius of curvature of wavefronts. For a Gaussian beam, beam radius $w(z)$ varies along the propagation direction as

$$w(z) = w_0\sqrt{1 + (\frac{z}{z_R})^2}$$

Rayleigh length is the length over which the beam propagates like a plane wave (without divergence) and is given by $z_R = \frac{\pi w_0^2}{\lambda}$. The radius of curvature of wavefronts follows the relation $R(z) = z[1 + (\frac{z_R}{z})^2]$.
Taking beam waist position to be the origin of the coordinate system, we can rewrite (1.5) at the entrance plane of nonlinear medium (r, z_0) as

$$E(r,z_0) = E(0,z_0)\exp(-\frac{r^2}{w(z_0)^2})\exp(-i\frac{kn_0r^2}{2R(z)}) \quad (2.5)$$

The intensity of Gaussian beam is written as

$$I(r) = I(0)e^{\frac{-2r^2}{w_0^2}} \quad (2.6)$$

where $I(r)$ is the intensity at radius r from the center of the beam. $I(0)$ is the intensity at the center of the beam and is equal to $\frac{2P}{\pi w(z)^2}$ (P being the power).

We rewrite (2.1) as a function of beam radius

$$n_e(r) = n_{0e}(r) + n_{2e}(r)I(r) \tag{2.7}$$

In general, $n_{0e}(r)$ is taken as a constant. Excluding thermal convection, $n_{2e}(r)$ can also be taken as a constant (thermal convection is one of the governing factors of $n_{2e}(r)$ though, as we shall study later). (2.1) gets modified to

$$n_e(r) = n_{0e} + n_{2e}I(r) \tag{2.8}$$

The phase shift $\phi(r)$ comprises of two terms $\phi_L(r)$ (linear) and $\phi_{NL}(r)$ (nonlinear). $\phi_L(r)$ which is equal to $\dfrac{kn_0r^2}{2R}$, is associated with the wavefront curvature. We calculate now, the nonlinear phase shift $\phi_{NL}(r)$. It can simply be related to the change in nonlinear refractive index as

$$\phi_{NL}(r) = \frac{2\pi n_{0e}}{\lambda}\int_{z_0}^{z_0+L}\Delta n(r,z)dz \tag{2.9}$$

$\Delta n(z,r)$ is related to n_{2e} as

$$\Delta n(r,z) = n_{2e}I(r,z) \tag{2.10}$$

Assuming that the sample medium is thin, the change in nonlinear refractive index (2.10) becomes independent of the propagation coordinate. Substituting (2.10) in (2.9), we get,

$$\Delta\phi(r) = \phi_{NL}(r) = \frac{2\pi n_{0e}n_{2e}}{\lambda}I_0Le^{\dfrac{-2r^2}{w_0^2}} \tag{2.11}$$

We see that the nonlinear phase shift $\phi_{NL}(r)$ has a Gaussian profile. Two wavefronts at points r_1 and r_2, respectively, propagating along z-direction will differ in phase. Since these two radial wavefront possess the same transverse wavenumber

$$k_\perp = \frac{d\Delta\phi(r)}{dr} \tag{2.12}$$

, they will interfere to form either maxima or minima, depending on,

$$\Delta\phi(r_1) - \Delta\phi(r_2) = m\pi \tag{2.13}$$

where m is an integer. m will be even for a maxima and odd for a minima. We can calculate the maximum phase shift in far field as

$$\Delta\phi(0) - \Delta\phi(\infty) = 2N\pi \tag{2.14}$$

Using (2.11), we get,

$$n_{2e} = (\frac{\lambda}{2n_0 L})\frac{N}{I} \tag{2.15}$$

The outermost ring in the diffraction pattern formed in far field has the greatest phase variation gradient ($k_\perp$),

$$k_\perp = [\frac{d\Delta\phi(r)}{dr}]_{max} \tag{2.16}$$

So, the maximum half diffraction angle (half cone angle) θ_H is given by

$$\tan\theta_H = \frac{1}{k}[\frac{d\Delta\phi(r)}{dr}]_{max} \tag{2.17}$$

For small angle θ_H,

$$\theta_H = \frac{1}{k}[\frac{d\Delta\phi(r)}{dr}]_{max} = n_{2e}c \tag{2.18}$$

where c is equal to $[\frac{8rIl}{w_0^2}e^{\frac{-2r^2}{w_0^2}}]_{max}$

Thus, from (2.18), we see that the half cone angle is independent of n_{0e} [3,4,].

2.4 Analogy With Classical Optics

We can describe the SSPM phenomenon caused by a Gaussian beam as diffraction of light through a circular aperture. First, let us consider diffraction of light as it passes through an arbitrary aperture as shown in figure. The aperture lies in $\zeta\eta Z$ coordinate plane and the screen is z distance away from the aperture along the Z-axis in XYZ coordinate plane. Acording to Hygen's principle, each point at the aperture behaves as point source for the incident light and emits spherical wave $E(\zeta, \eta)$ upon incidence. The phase difference in between these

spherical waves emitting from different point sources will lead to interference and the resultant electric field at a point $P(x, y)$ can be written as

$$E(x,y) = C_1 \int_{\eta=0}^{\infty} \int_{\zeta=0}^{\infty} U(\zeta,\eta)(\frac{e^{ik\zeta}}{r})d\zeta d\eta \tag{2.19}$$

Under far field approximation ($z >> \frac{k}{2}(\zeta^2 + \eta^2)$), this can be written as

$$E(x,y) = \frac{e^{ikz}}{i\lambda z} e^{\frac{ik}{2z}(x^2+y^2)} \int_{\eta=0}^{\infty} \int_{\zeta=0}^{\infty} E(\zeta,\eta) e^{\frac{-ik}{z}(x\zeta+y\eta)} d\zeta d\eta \tag{2.20}$$

In case of circular aperture, (2.20) is modified to

$$E(P) = \frac{e^{ikz}}{i\lambda z} e^{\frac{ik}{2z}(x^2+y^2)} 2\pi E_0 \int_{r=0}^{\infty} J_0(kr\theta) \exp(-\frac{r^2}{w(z)^2} - i(\frac{kn_0 r^2}{2R(z)} + \Phi_{NL}))rdr \tag{2.21}$$

where $J_0(kr\theta)$ is $zero^{th}$ order Bessel function.
In case of SSPM, the intensity distribution at point P is given by

$$I = I_0 | \int_0^{\infty} J_0(kr\omega) \exp(-\frac{r^2}{w(z)^2}) \exp(-i\frac{kn_0 r^2}{2R(z)}) \exp(-i\Phi_{NL}) rdr|^2 \tag{2.22}$$

where $I_0 = 4\pi^2 |\frac{E(0,z)e^{-\alpha L}}{i\lambda d}|^2$. $e^{-\alpha L}$ attributes to the absorption of light by medium and d is the distance between medium and screen [9].

2.4.1 Thermal Convection

In nonlinear optical phenomena, the incident electric field of high intensity interacts strongly with the medium. These high intensities generate thermal heating. In fact, thermal heating plays important role in SSPM experiment. When the light passes through the liquid medium, a part of its intensity is absorbed. Due to absorption, significant amount of heat is generated. This leads to convection current generation in sample, due to which liquid layer from the center of beam start rising upwards. The heat escapes from the central region, creating a temperature gradient and hence leading to density redistribution of the sample. This phenomenon causes a refractive index gradient of the system with respect to temperature $(\frac{dn}{dT})$ [1]. Graphene possesses high thermal conductivity and

optical absorption coefficient, which hints at strong thermal convection during SSPM in graphene dispersion.

The refractive index gradient depends on the internal structure of the material and depending on sign of $\frac{dn}{dT}$, the medium behaves either like a converging or a diverging lens. Evolution of the thermal lens effect is also a medium characteristic.
Variation of refractive index with temperature can be modeled as

$$n = n_0 + (\frac{dn}{dT})\Delta T \tag{2.23}$$

where ΔT is temperature induced due the laser beam.
We can model the temperature profile of ΔT using heat transport equation,

$$\rho C \frac{\delta \Delta T(x,y,t)}{\delta t} - \nabla^2 K(\Delta T(x,y,t)) = Q(x,y) \tag{2.24}$$

where ρC is the heat capacity per unit volume and $Q(x,y) = \alpha I(x,y)$ is the absorbed heat from laser. We solve this equation in steady state condition later in *Chapter*3 to find out the thermal effect in SSPM.

Modeling dynamic heat transport equation during SSPM remains a part of immediate future plan.

Chapter 3

Results and Discussion

In chapter 2, we became familiar with several nonlinear optical properties of materials and the physics of spatial self-phase modulation (SSPM). Now we proceed with the experimental analysis part. In this chapter, we discuss the sample preparation method, different optical set-up construction and measurement techniques. Then we analyze and discuss the obtained results.

3.1 Sample Preparation

3.1.1 Graphene

Graphene (few layer) was prepared by electrochemical exfoliation of graphite sheet (thickness $0.5mm$). We used an electrolyte solution of 0.1M $(NH_4)_2SO_4$ in water and graphite as both cathode and anode for electrolysis (figure 3.1).

When DC voltage of $+10V$ was applied to a graphite electrode, the graphite flakes began to dissociate and got dispersed into the solution. The process continued for 2 hours and at the end a dark black solution was obtained. The solution was sonicated for 2 hours in order to break them further and was left overnight for heavier particles to settle down. Next day, top 3/4 volume of solution was washed repeatedly with water followed by centrifugation at 7000rpm. Afterward, the product was dried in vacuum for a couple of days. We made 0.1mg ml^{-1} solution of obtained graphene in a common organic solvent DMF (Di Methyl Formaldimide). The color of this solution is light black, and the solution stays stable for weeks (very small amount of particles get settled) and the color of solution still remains slight black. This indicates the presence of graphene in our solution.

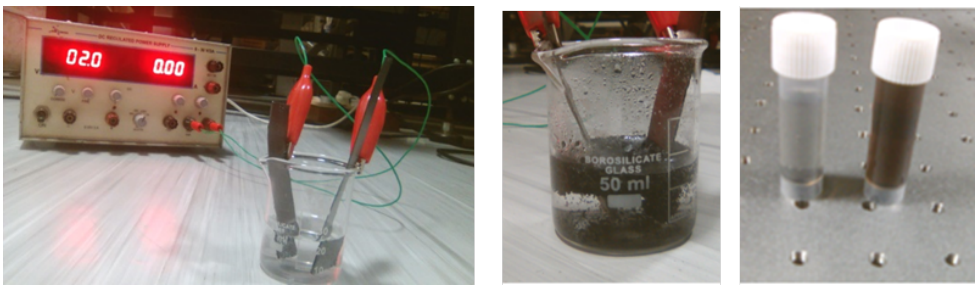

Figure 3.1: a) Electrolysis of graphite at a constant DC voltage. b) Solution after exfoliation with clear view of lighter graphene particles near the top surface and unexfoliated graphite at bottom. c) Dispersed graphene (left) and graphene oxide(right) in DMF.

Mechanism

When bias voltage is applied, it results in reduction of water at the cathode, creating hydroxyl ions (OH^-) that act as a strong nucleophile in the electrolyte. The (OH^-) ions attack the nucleophillic graphite site at anode. Oxidation at these sites leads to depolarization and expansion of the graphite layers. This process produce gaseous species such as (SO_2), O_2 etc, which exert large forces on the graphite layers to separate weakly bonded layers from one another [5].

Several research wors have shown that about 85% of the graphene particles are less than 4 layers. The charecterization results for the prepared sample for our experiment is still awaited, yet, we expect similar results on basis of its stable dispersion for weeks.

3.1.2 Graphene Oxide

Graphene Oxide (GO) was prepared by modified Hummer's method. We thank Dr. Venkataramanan's Research Group, IISER Kolkata for providing us the prepared GO powder. GO was dispersed in DMF with a concentration of $0.1 mg ml^{-1}$. This solution is also found to be stable for weeks, indicating good quality of the product.

3.2 Knife-Edge Experiment

Knife-edge experiment is a general and method to find out the spot size of a laser beam. The schematic set up for this experiment is shown in figure. We use a lens to focus the laser beam propagating along z-direction at the edge of knife (in our case, edge of a thin blade). The knife-edge is mounted on a translational stage such that it can move both along the beam direction (z-direction) and orthogonal (x-axis) to it.

We keep the position of knife-edge fixed along the propagation direction of laser beam, while gradually moving it in the direction orthogonal to propagation. Initially, the knife-edge is outside the beam spot (not intersecting its path). As it is moved inwards (towards the beam), it overlaps (blocks) a finite portion the beam spot. It eventually crosses through the laser spot and blocks it completely. A photo-detector placed behind the knife-edge measures incoming intensity (voltage). Initially, the detector can detect completely undisturbed intensity of the beam. As the knife-edge moves into the laser beam, only a fraction of intensity is detectable. This fraction keeps decreasing and goes to minimum when the knife-edge completely blocks the laser beam (figure 3.2).

The measured intensity by the photo-detector as a function of position of knife-edge is shown in figure. This is evident that the region of the plot whose slope is nonzero, is in fact the diameter of the beam. Derivative of the measured intensity with respect to position should give a Gaussian profile, and is with standard Gaussian function $F(x) = F_0 \exp[-2\frac{(x-x_c)^2}{r^2}]$ From the fit, we get the beam radius r. We obtain the beam radius at different z-positions on either side of the focus. Figure shows the beam radius profile along z-axis (focal point is taken as zero). This is fitted using the relation

$$r(z) = r_0\sqrt{1 + (\frac{(z-\delta)}{z_0})^2} \tag{3.1}$$

to get the beam spot size. Here r_0 is the beam waist (spot size at the focus), $z_0 = \pi r^2/\lambda$ is the Rayleigh length and δ is the correction in focal position.
Performing Knife-edge experiment with a cw laser of wavelength $489nm$, gives us the value of beam waist $r_0 = 28\mu m$.

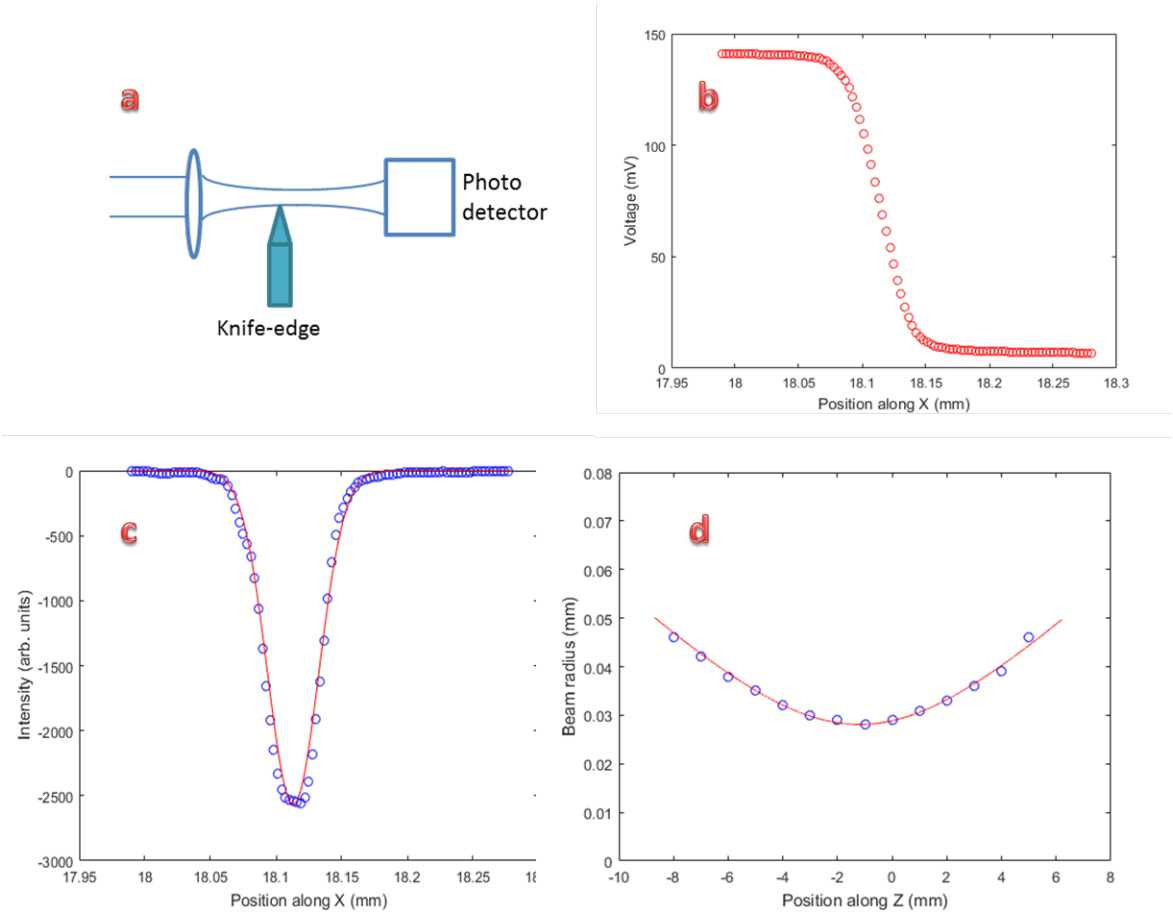

Figure 3.2: a) Experimental set up for knife edge experiment. b) signal detected by the photo-detector. c) Gaussian fit of the intensity profile obtained by differentiating data from (b). d) beam radius plot at different position relative to focus point. Minimum radius is at focus.

3.3 SSPM

In our experiment, we studied the nonlinearity in graphene and graphene oxide (GO) using ultraviolet, visible and near-infrared continuous wave laser beams. The laser was focused using a lens of focal length $10cm$. The solution (graphene and GO, both having concentration $0.1mgml^{-1}$) was taken in a $10mm$ quartz cuvette and placed before focus ($R < 0$). The front face of cuvette was placed $68mm$ from the lens. Continuous wave Lasers with 4 different wavelength ($\lambda =$

$403nm, 489nm, 661nm$ and $791nm$ respectively,) were used in our experiment. Beam waist for all these lasers were calculated using Knife-edge experiment and found to be $28\mu m$. The laser spot size at the front face of cuvette was estimated to be $114\mu m, 161\mu m, 173\mu m$ and $277\mu m$ for $\lambda = 403nm, 489nm, 661nm$ and $791nm$, respectively. Far field intensity pattern of the transmitted laser beam was observed at a distance of $126cm$ from the cuvette. We used high resolution Logitech web camera with 30 frames per second to record the diffraction pattern. Afterwards, we also used Sony digital camera with remarkable 1000 frames per second to study diffraction dynamics in details. Experimental set up is shown in figure 3.3

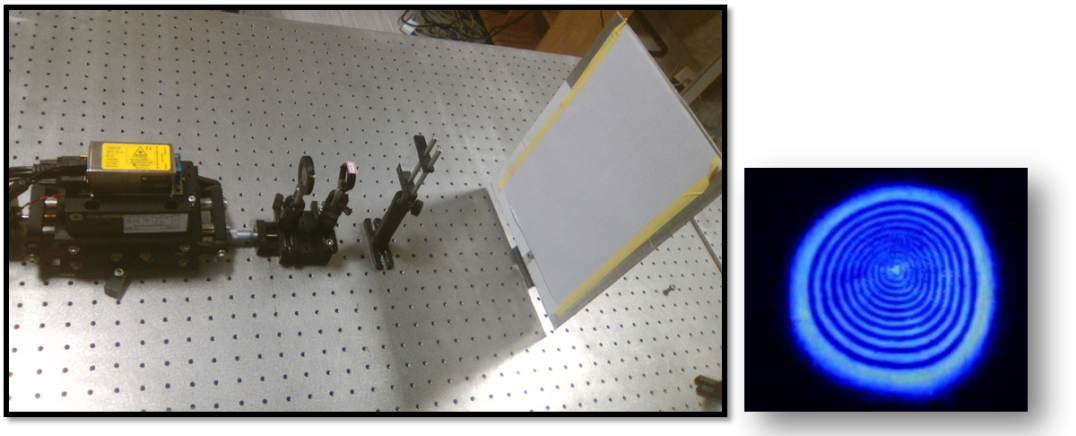

Figure 3.3: a) Experimental set up used for performing SSPM experiment. Obtained diffraction pattern is on the right side.

3.3.1 Results and Discussion

The laser beam is made to propagate through the sample using a manual shutter at time t=0 and resulting diffraction pattern in far field is recorded using camera. In order to justify that the non-linearity occurs solely due to graphene, we repeated the experiment by replacing graphene dispersion with DMF solution. No such diffraction pattern was observed which shows that the solvent doesn't play any role in non-linearity. Figure shows the observed diffraction pattern in

graphene at power at 489nm.

We recall the far field intensity distribution expression (2.22) from the previous chapter. A simulation of the intensity distribution (corresponding to experimental conditions as in figure 3.4*a*) is shown in figure, adjacent to experimentally observed intensity distribution (figure 3.4*b*). This shows a good match between experimentally and theoretically obtained pattern.

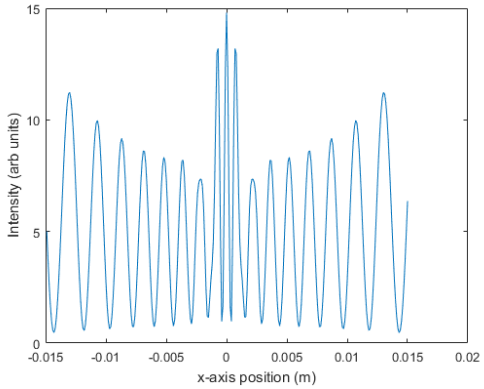

(a) simulation for obtaining intensity profile using (2.22).

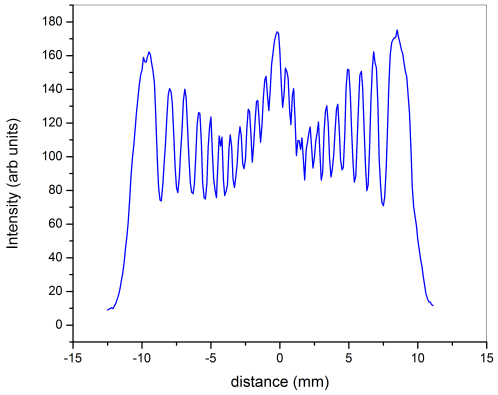

(b) Experimentally observed intensity profile.

Figure 3.4

Intensity dependent diffraction pattern is observed in different wavelength regime. Figure 3.5 shows the pattern in graphene dispersion at different incident laser power at 489nm. Number of rings and diameter of the outer ring both increase with power.

Similar ring patterns are observed in four different wavelength regimes with increase in number of rings as one goes into lower wavelength regime (figure 3.6).

We now proceed to calculate the nonlinear refractive index of graphene dispersion. Recall

$$n_{2e} = (\frac{\lambda}{2n_0 L})\frac{N}{I} \tag{3.2}$$

We calculate n_2 from the slope of number of rings (N) vs intensity (I) plot. N vs I plots for graphene and graphene oxide in different wavelength regime are

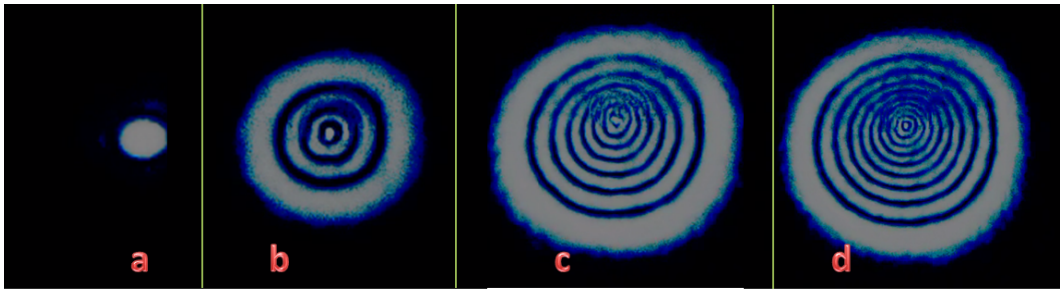

Figure 3.5: Ring patterns in graphene at different power. (a) No rings were observed at $3.75mW$, number of rings increase at $22.1mW$ (b), $35mW$ (c) and $46mW$ (d).

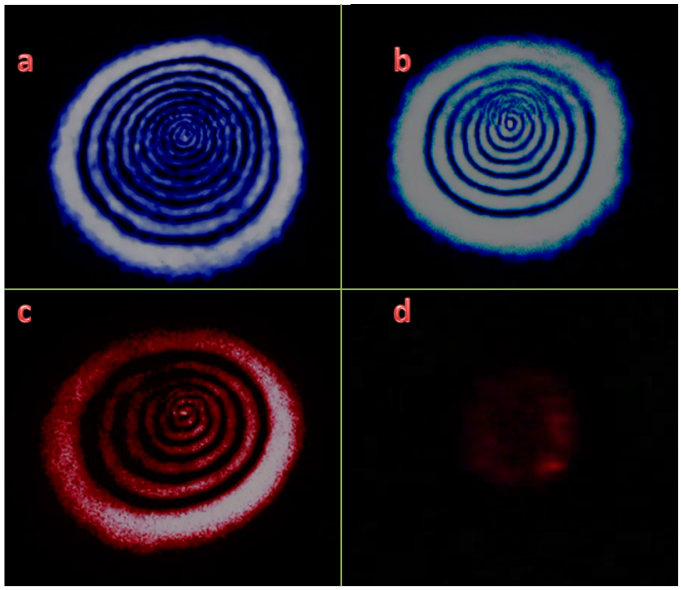

Figure 3.6: Number of rings decrease as wavelength increases. ($403nm$ (a), $489nm$ (b), $661nm$ (c) and $791nm$ (d). Power is fixed at $35mW$.

shown in figure 3.7. For our experiment, cuvette path length L is 10mm and linear refractive index of solvent DMF n_0 is 1.43. We calculated the value of n_2 at $489nm$ wavelength to be $3.8x10^{-10\pm1}$ m^2W^{-1}. This magnitude matches quite well with the reported value by Y. L. Wu *et. al.* [6].

Bulk nonlinear susceptibility of graphene and graphene oxide can be calculated

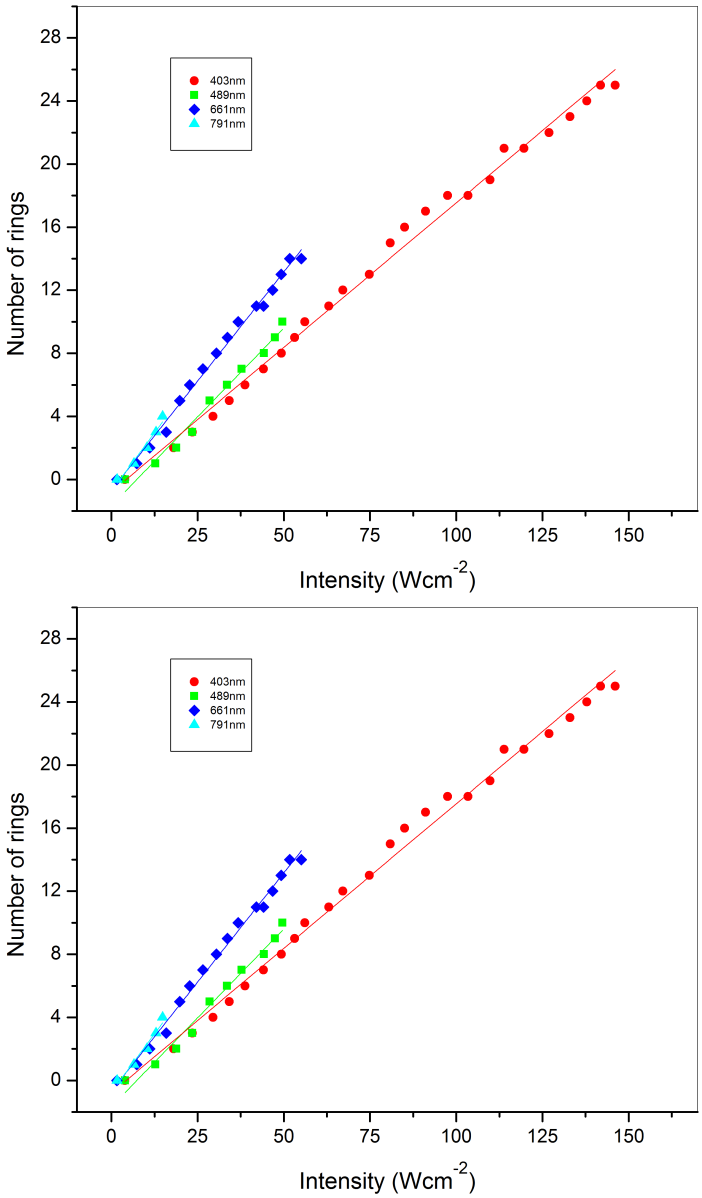

Figure 3.7: Number of rings vs Intensity plot for Graphene oxide (above) and graphene (below).

using the relation

$$n_{2e}(\frac{m^2}{W}) = \frac{395}{n_0^2}\chi^3(esu) \tag{3.3}$$

χ^3_{bulk} is approximately related to monolayer χ^3 by

$$\chi^3_{bulk} = M^2 \chi^3_{monolayer} \tag{3.4}$$

where $M = \dfrac{cVN_A}{(S/a^2)}$ is the number of monolayer graphene in dispersion [8]. c and V are the concentration and volume of the solution, respectively. S is the cross sectional area of cuvette and a is the lattice constant of graphene. In our experiment, $0.8ml(0.1mgml^{-1})$ solution was used in a $10mmx10mm$ cuvette. Substituting these value, we find $M \approx 300$ for our experiment and the nonlinear susceptibility of monolyer graphene was found out to be $1.9x10^{-9}\ ^{pm1}esu$.

3.4 Origin of SSPM

There are two competing theories for origin of SSPM in graphene. Thermal lens effect is an earlier proposed theory, which attributes the change in refractive index of a medium to its increasing temperature as it absorbs the incident light. However, a recently proposed theory predicts electronic origin of the SSPM phenomenon in graphene. In previous chapter, we have discussed the thermal convection process and it contribution to nonlinearity in a medium.

Here we discuss the other theory in brief, and based on the experimental results, we conclude that the thermal effect dominates over electronic effect to cause nonlinearity in graphene.

3.4.1 Coherence theory

Coherence theory, which predicts electronic origin of nonlinearity in graphene, was first proposed by R. Wu. et. al. in 2011. They ascribe the nonlinearity in graphene to the reorientation and alignment of suspended graphene sheets in dispersion under electromagnetic field due to light. The monolayer or few layer graphene sheets are freely suspended in the solution and can be treated as independent domain. When the laser light passes through a sheet, electrons in valence band absorb energy to excite into conduction band and undergo subsequent relaxation. The relaxation process is of the order of picoseconds. Movement of electrons and holes move in opposite directions makes the graphene sheets polarized. Initially, there might be some random angle between two

polarized graphene sheets depending on their interaction energy. In order to minimize this energy, the graphene sheets will re orientate themselves, which causes nonlinearity. Because these sheets are independently suspended, charge carriers situated on different different sheets are in phase and contribute constructively to the SSPM pattern [4]. Along with this, the band structure of graphene and high mobility of charge careers allow us to see ring pattern at very low threshold intensity (3 Wcm^{-2} in our experiment).

3.4.2 Evidence of Thermal Convection

When the laser beam passes through a solution, it induces local heating of the molecules, which leads to convection currents. These currents will displace the liquid layers due to which heat will escape from the beam region and an asymmetrical temperature distribution will be created. Consequently, redistribution of local density occurs leading to change in refractive index of the medium. Experimental observation of thermal convection can be seen through time evolution of ring pattern (figure 3.8). We see that in initial phase of ring formation, the size of ring (vertical and horizontal diameter of the outermost ring) evolves uniformly to reach its maximum, which is followed by a vertically downward shrink in its upper half structure till it attains a steady state. Corresponding time evolution of outer ring diameter is shown in figure 3.9.

When the nonlinear medium gets heated by laser light, the time it takes to convert the laser energy into thermal energy is attributed to the time the diffracted beam takes to acquire a maximally uniform ring pattern. Afterwards, convection currents give rise to asymmetrical temperature gradient and hence local density distribution. The heated layers of dispersion lift upwards and are replaced by relatively denser layers that move towards the center of the beam. This is the reason for vertical shrink in the upper half portion of rings. After some time, when the temperature distribution reaches steady state, there is no further shrinkage in the structure [8].

3.5 Dominance of Thermal Effect

We analyze experimentally, the significance of thermal convection in SSPM. Figure 3.10 pictorially represents shrink in diffraction ring pattern. θ_H is half

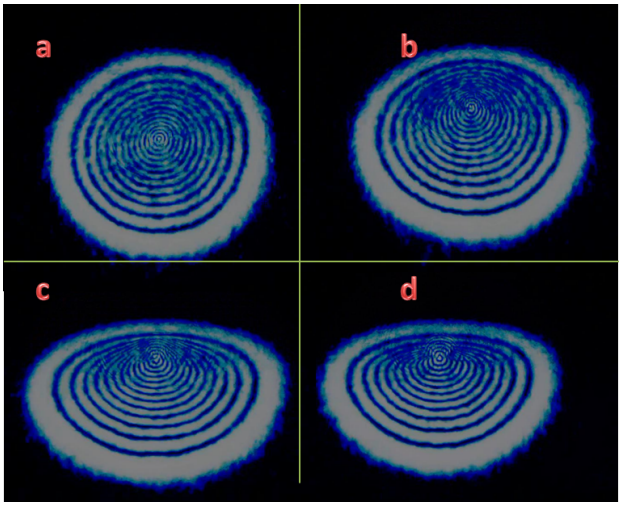

Figure 3.8: (a) At $35mW$ power and $489nm$, ring pattern is maximally uniform at $t = 0.25s$. (b) First observation of deformation at $0.3s$. Pattern at $0.4s$ (c) and at $1s$ (d).

the angle made by outermost diameter with the exit point of cuvette along the direction of propagation of beam. θ_D is the angle by which the ring structure deforms. From (2.18), we see that

$$\theta_H = cn_{2e} \tag{3.5}$$

so that

$$\frac{\theta_D}{\theta_H} = \frac{\Delta n_{2e}}{n_{2e}} \tag{3.6}$$

Figures 3.11 and 3.12 show the variation of θ_H and θ_H for graphene and graphene oxide, respectively, at 489nm. From the plot (figure 3.13) of fractional change in refractive index, we estimate that maximum change in nonlinear refractive index of graphene is 0.67. This concludes that the thermal effect in SSPM is quite significant [3].

3.5.1 Other observations

We can write heat transport equation for temperature profile as

$$\rho C \frac{\delta \Delta T}{\delta t} - \kappa \nabla^2 (\Delta T) = \alpha I \tag{3.7}$$

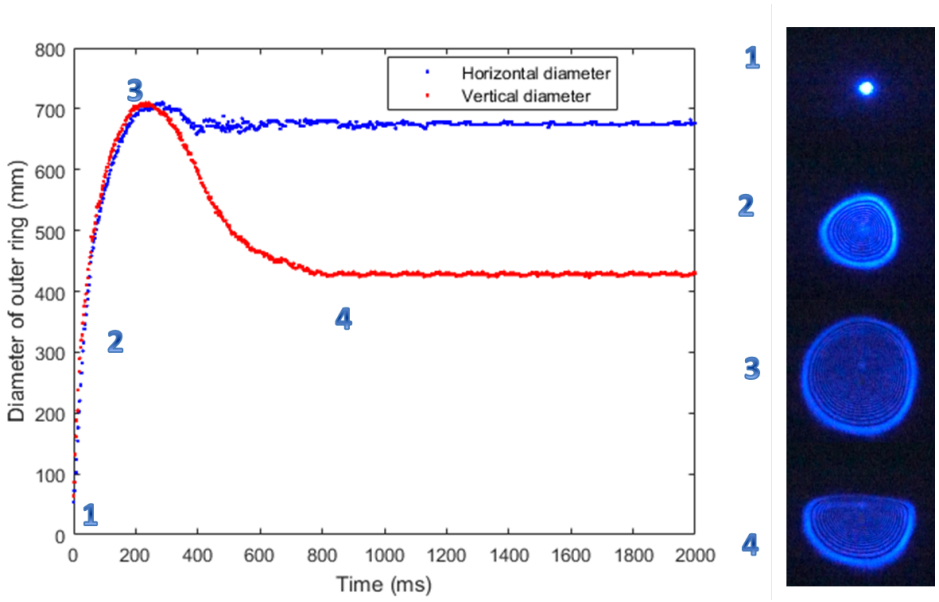

Figure 3.9: Time evolution of out ring diameter in graphene oxide at laser power $489nm$ and power $80mW$.

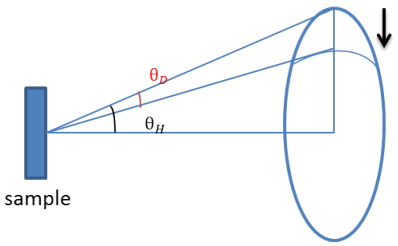

Figure 3.10: Schematic diagram representing the maximum half cone angle θ_H and destortion angle θ_D, respectively.

where ΔT is the temperature rise in the medium, κ is thermal conductivity, α is the absorption coefficient and ρC is the heat capacity per unit volume [1]. We can find the maximum temperature difference in steady state by approximating $\nabla^2(\Delta T_{max}) = -\dfrac{T_{max}}{R^2}$ as

$$T_{max} = \frac{\alpha I_{max} R^2}{\kappa} \tag{3.8}$$

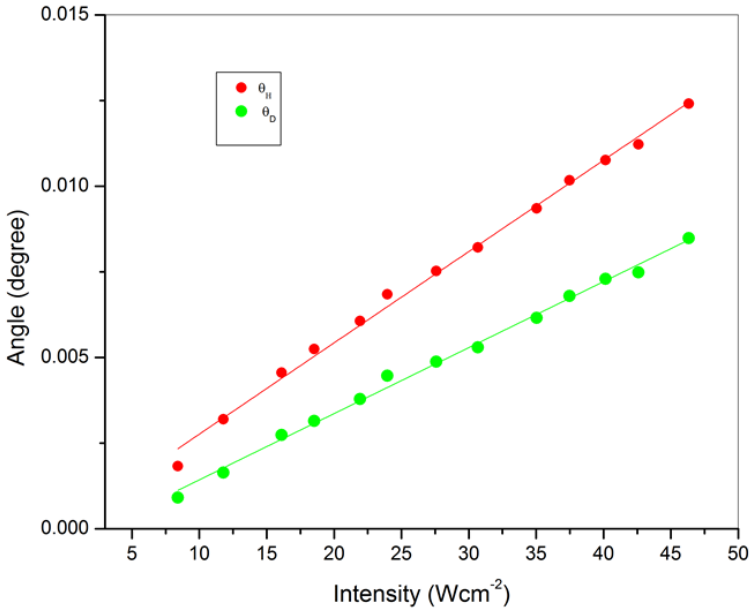

Figure 3.11: Variation of half cone angle and distortion angle in graphene with respect to intensity at $489nm$.

Using thermal nonlinear refractive index expression,

$$\Delta n_{th} = (\frac{dn}{dT})T \tag{3.9}$$

we obtain the relation

$$n_2^{thermal} = (\frac{dn}{dT})\frac{\alpha R^2}{\kappa} \tag{3.10}$$

A theoretical plot of this equation using standard values of constants (figure 3.14) shows that the thermal nonlinear refractive index is maximum at focus. This can be understood from simple fact that at focus, the cross sectional area of Gaussian beam is minimum that means maximum intensity and hence maximum thermal effect. In our experiment, when we used pulse laser at $780nm$ to observe SSPM in graphene by placing sample at different position from focus, we observe that the thermal effect at focus is so large that it dominates SSPM. There is

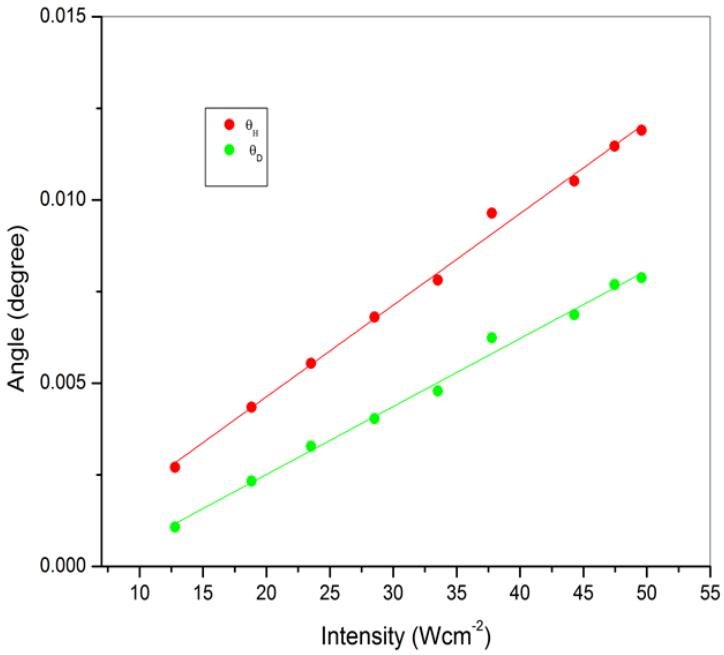

Figure 3.12: Variation of half cone angle and distortion angle in graphene oxide with respect to intensity at $489nm$.

huge divergence of light and eventually we do not see any SSPM pattern.

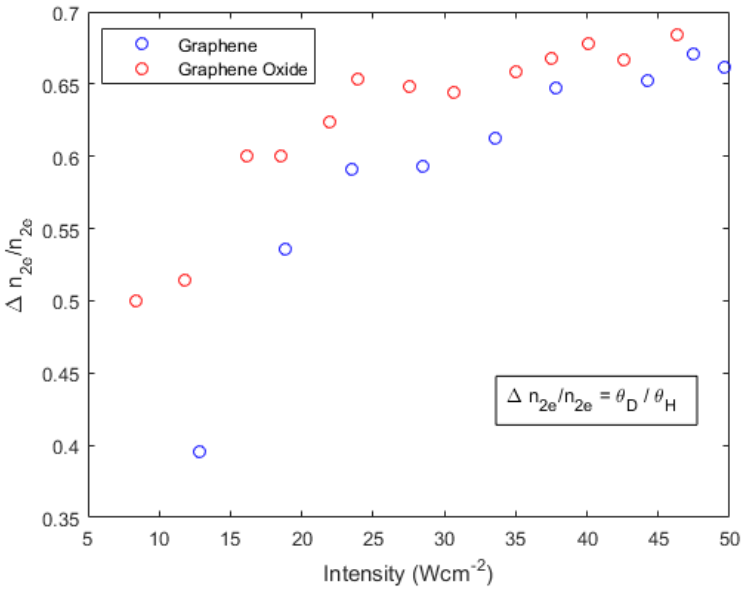

Figure 3.13: Plot shows the fractional change in nonlinear refractive index of graphene and graphene oxide.

3.5.2 Fine structure rings

We have seen earlier in chapter 1 that the phase factor for a Gaussian beam consists of both linear and nonlinear term. Linear phase term arise due to wavefront curvature, while the nonlinear term corresponds to the medium. Far above the threshold limit of nonlinearity the, nonlinear phase term dominates the linear phase term, while just above the threshold limit, both the phase terms are comparable, so, they interfere to give fine tiny ring structure (in addition to usual diffraction pattern). In our experiment, in order to avoid large thermal effect, we placed sample at a distance 32 mm before the focus of a 10cm lens. At such large distance, the wavefront curvature of beam is high and the linear phase is comparable to the nonlinear phase, so, they interfere to give small rings (figure 3.15).

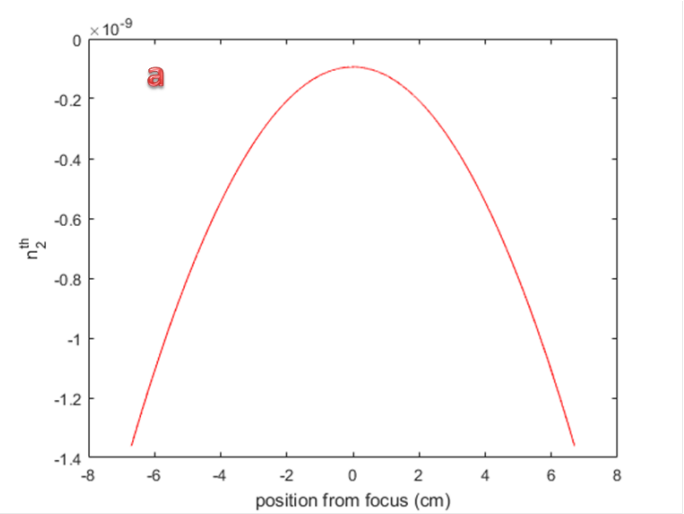

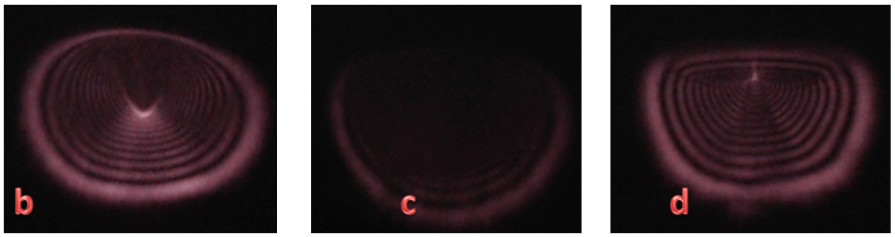

Figure 3.14: a) Theoretical plot shwing that the thermal nonlinear refractive index in any liquid medium is highest at focus. A well observed diffraction pattern in graphene at 15 mm before (a) and 15mm after focus (b). Huge divergence is observed at focus (b) due to thermal effect.

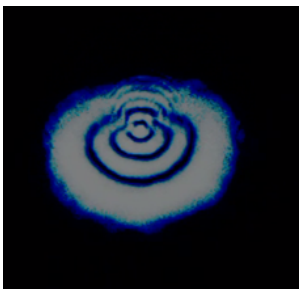

Figure 3.15: Few tiny rings can be seen in the diffraction pattern when graphene dispersion is placed far from focus ($\lambda = 403nm$).

Chapter 4

Conclusion and Future Plan

The presented work was the first part of our work plan where the main aim was to study nonlinear optical nonlinearities in graphene by SSPM and to estimate the impact thermal effect in SSPM in graphene. Based on our experimental results, we estimated the value of nonlinear refractive index and nonlinear susceptibility of graphene, which match quite well with earlier reported values.

We also observed that the thermal effect due to laser intensity dominates the SSPM phenomenon in graphene and graphene oxide. However, dynamic study of thermal convection is yet to be performed. Thermal effect can be studied in details if we compare the SSPM in graphene with cw laser and with pulse laser. We shall look forward to this in immediate future. Time resolved SSPM might help in distinguishing thermal effect from electronic effect in SSPM. We have also planned to study Z-scan and time resolved Z-scan studies to understand third order nonlinearities from another point of view. I hope that I would be able to understand the physics behind optical nonlinearities in graphene in great details through this thesis.

I thank Dr. Bipul Pal, Dr. Bhavtosh Bansal, Samrat Roy, Shruti J. S. and other lab members for their important contribution while carrying this project and IISER Kolkata for providing me a platform to carry my MS project. I also thank Dr. V Mahalingam' research lab for their help in preparing sample, and Dr. Ayan Banerjee's research lab for providing us high frame rate camera.

Bibliography

[1] Robert W. Boyd, *Nonlinear Optics*, 978-0-12-369470-6., Elsevier, London, 2008. 3rd edition.

[2] A. K. Geim, K. S. Novosolov, Nature Materials, 6 (2007).

[3] Gaozhong Wang et. al., Applied Physics Letters 104, 141909 (2014).

[4] Rui Wu, et. al., Nano Letters, 11, 5159–5164 (2011)

[5] Khaled Parvez, , et. al., Journal of the American Chemical Society, 136, 6083–6091 (2014).

[6] Y. L. Wu et. al., Applied Physics Letter 108, 241110 (2016).

[7] Wenhui Wang et. al., Scientific Reports, Nature Communications (2017).

[8] Yahan Wang, et. al., Nanoscale, 9, 3547–3554 (2017).

[9] Luogen Deng, et. al., Journal of Optics A: Pure and Applied Optics, 7 409 (2005).